

Unraveling the Morphology–Function Relationships of Polyamide Membranes Using Quantitative Electron Tomography

Xiaohui Song,^{†,°} John W. Smith,^{†,°} Juyeong Kim,^{†,‡,∇} Nestor J. Zaluzec,[⊥] Wenxiang Chen,^{†,‡} Hyosung An,^{†,‡} Jordan M. Dennison,[§] David G. Cahill,^{†,‡} Matthew A. Kulzick,[#] and Qian Chen^{*,†,‡,§,||}

[†]Department of Materials Science and Engineering, [‡]Materials Research Laboratory, [§]Department of Chemistry, and ^{||}Beckman Institute for Advanced Science and Technology, University of Illinois at Urbana-Champaign, Urbana, Illinois 61801, United States

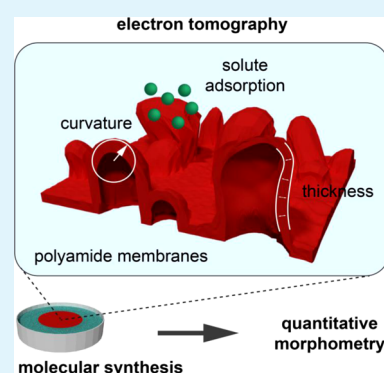
[⊥]Photon Sciences Division, Argonne National Laboratory, Argonne, Illinois 60439, United States

[#]BP Corporate Research Center, Naperville, Illinois 60563, United States

Supporting Information

ABSTRACT: An understanding of how complex nanoscale morphologies emerge from synthesis would offer powerful strategies to construct soft materials with designed structures and functions. However, these kinds of morphologies have proven difficult to characterize, and therefore manipulate, because they are three-dimensional (3D), nanoscopic, and often highly irregular. Here, we studied polyamide (PA) membranes used in wastewater reclamation as a prime example of this challenge. Using electron tomography and quantitative morphometry, we reconstructed the nanoscale morphology of 3D crumples and voids in PA membranes for the first time. Various parameters governing film transport properties, such as surface-to-volume ratio and mass-per-area, were measured directly from the reconstructed membrane structure. In addition, we extracted information inaccessible by other means. For example, 3D reconstruction shows that membrane nanostructures are formed from PA layers 15–20 nm thick folding into 3D crumples which envelope up to 30% void by volume. Mapping local curvature and thickness in 3D quantitatively groups these crumples into three classes, “domes”, “dimples”, and “clusters”, each being a distinct type of microenvironment. Elemental mapping of metal ion adsorption across the film demonstrates that these previously missed parameters are relevant to membrane performance. This imaging–morphometry platform can be applicable to other nanoscale soft materials and potentially suggests engineering strategies based directly on synthesis–morphology–function relationships.

KEYWORDS: synthesis–morphology–function relationship, 3D reconstruction, polymer electron tomography, polyamide membranes, nanoscale morphometry



INTRODUCTION

Biological morphogenesis, or the way in which living systems develop structure, has inspired a tremendous variety of strategies to construct synthetic nanomaterials with complex and functional morphologies. For example, taking cues from how cells utilize intermolecular interactions to build membranes and organelles, block co-polymers have been engineered to self-assemble structures ranging from spherical micelles^{1,2} and patterned two-dimensional (2D) arrays^{3–5} all the way to three-dimensional (3D) bicontinuous phases.⁶ Inspired by the ways that living systems use chemical synthesis to construct the ornate microscopic surfaces of diatoms and the coloration patterns of fish and shells,^{7–9} phase separation and reaction–diffusion processes have been manipulated to grow metallic nanoparticles with nanostructured cores and surfaces^{10,11} and intricate silica–carbonate “biomorphs”.¹² However, when it comes to utilizing these chemical strategies at the nanoscale, predictive design is challenging, largely because of the difficulty associated with investigating the

convoluted, often nonperiodic nanostructures that can emerge from synthesis. In particular, because characterizing the nanoscale 3D structure of such materials is difficult, especially for soft materials, quantitative understanding of their synthesis–structure and structure–function relationships is limited.

Thin-film composite (TFC) membranes are a prime example of this challenge. TFC membranes with polyamide (PA) separating layers play key roles in modern technologies for industrial and domestic water desalination, purification of chemicals and pharmaceuticals, and recycling of catalysts.^{13–16} These films commonly develop complicated and heterogeneous 3D structural features during synthesis, possibly due to local fluctuations in temperature or concentration during film formation.¹⁷ Because PA layers constitute the selective barrier

Received: November 27, 2018

Accepted: January 24, 2019

Published: January 24, 2019

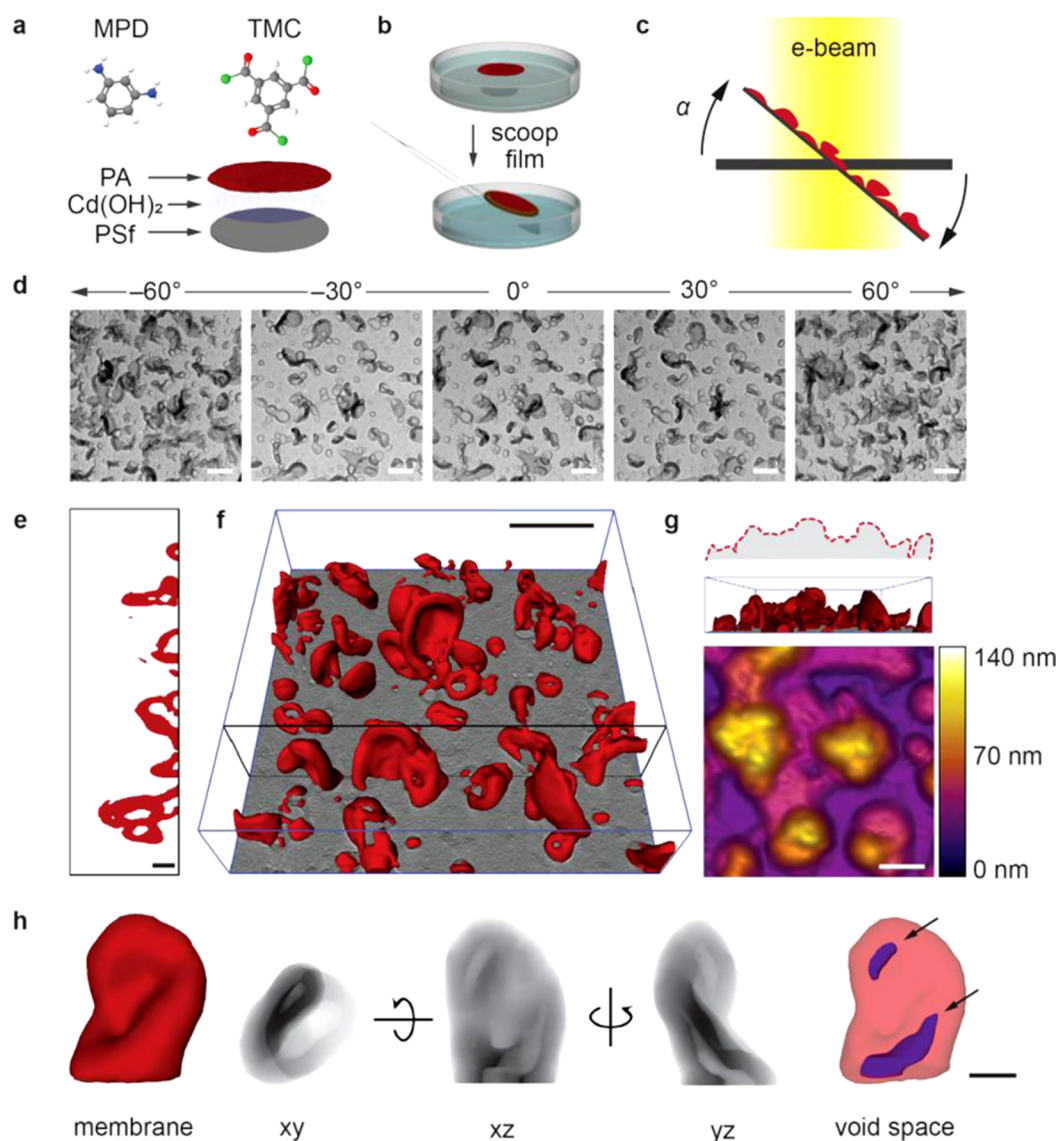


Figure 1. Synthesis and electron tomography of a PA film. (a) Interfacial polymerization of MPD and TMC on a sacrificial cadmium hydroxide ($\text{Cd}(\text{OH})_2$) layer and a PSf support was used to produce freely floating PA films that can be scooped onto a TEM grid (b). In the molecular models, gray represents carbon, white hydrogen, blue nitrogen, red oxygen, and green chlorine. (c) A schematic of tomography, which involves collecting projections from different viewing angles (α). (d) Five representative TEM images (out of 61 total) of the same PA film region taken at different tilt angles, which were used to determine a 3D image. (e) A 2D slice through the reconstructed 3D PA film (marked with the black border in (f)). (f) A full 3D view of the complete PA film before extensive image processing. (g) A side view of the reconstruction (middle) shows a rough film surface (traced schematically, top), which we also measured using AFM (bottom). (h) Individual crumples were semimanually segmented from the 3D dataset, from which various projections (xy , xz , yz), and interior details (void labeled in purple), could be resolved. Scale bars: 200 nm in (d), (f), and (g), 50 nm in (e) and (h).

to molecular permeation,¹⁸ such structures play an important role in the solvent permeability, solute rejection, fouling resistance, and mechanical strength of membranes.^{19,20} For example, previous work has shown that PA film thickness directly relates to the molecular diffusion length,^{21,22} such that thicknesses on the order of 10 nm are desirable to balance solvent flux with mechanical stability required for the high operating pressures used in nanofiltration and reverse osmosis.^{17,19,23,24} Features such as interior voids were also measured to affect performance, increasing water permeability by 5 times compared with an equivalent layer without voids.^{25,26} Nevertheless, understanding the complete nanoscale 3D structure of PA films has been met by challenges. For example, although interior features were shown to be

relevant to performance, techniques like scanning electron microscopy (SEM)^{19,27–29} and atomic force microscopy (AFM)^{18,29–31} can only resolve the topmost surface of PA films not their internal voids. In addition, bulk characterization^{32,33} or advanced statistical methods^{34,35} are not readily applicable because membrane features are heterogeneous and irregular. Tomography using focused ion beam SEM³⁶ and transmission electron microscopy (TEM)^{29,37} was recently used to obtain some 3D information in commercial PA membranes, but the internal voids and external morphology of membranes have not been examined simultaneously. Factors such as the dense packing of film nanostructures, low imaging contrast, and artifacts from resin fixation prevented voids from being fully resolved,^{29,36} and features such as film density and

thickness have only been measured using tomography in membranes with ultralow void fractions ($\leq 0.12\%$ by volume).³⁷

Here, we imaged and extensively quantified functionally relevant aspects of the 3D nanostructure of PA membranes, including interior details, using a morphological analysis platform integrating recent advancements from three different fields. First, we used a recently developed synthesis method to produce PA films on a sacrificial layer. PA films synthesized in this manner¹⁷ were demonstrated to have exceptional organic solvent filtration performance and mechanical robustness, making them ideal candidates as a model system for extensive 3D characterization. Another advantage here is that these films can be freed from extraneous supports and are stable in the absence of fixatives, improving image contrast and preventing artifacts that may arise from resin fixation. Second, we used low-dose electron tomography without staining to image and reconstruct the 3D morphology of individual crumples and voids in the PA film. Low-dose imaging prevents changes to the nanoscale morphology of films during the sustained imaging times required for tomography. Third, we adapted methods from the biological sciences for quantitative morphological analysis.^{38–40} Using this hybrid approach, we measured a series of functionally relevant morphological properties, some of which are inaccessible by other means. These parameters range from macroscopic details, such as the surface areas and mass-per-area of crumples and voids (which occupy up to 30% of crumples by volume), to nanoscale features, such as 3D maps of local curvature and local thickness, to topological features, such as crumple interconnectivity, all with nanometer resolution. On the basis of these measurements, the crumples in the PA film, although seemingly unrelated in shape, can be grouped into just three classes which we refer to as “domes”, “dimples”, and “clusters”. These classes correspond to distinct microenvironments, potentially with different local transport behaviors. These quantitative observations are consistent with a mechanistic picture of crumples formed from otherwise flat PA layers locally folding and collapsing onto one another during synthesis,^{19,23,24} hinting at the opportunity to engineer membrane nanostructure directly from synthesis conditions. Finally, in an effort to connect structure and performance, we used energy-dispersive X-ray spectroscopy in a scanning transmission electron microscope (STEM-EDXS)^{41–43} to investigate how representative solutes, the heavy metal ions zinc and lead, adsorb onto the crumpled regions of the PA film. We find that these species localize to features of the crumpled film not only in a manner that is sensitive to local nanostructural details but also in different ways, which may account for the distinct filtration behavior of these solutes observed experimentally.^{44,45}

We expect that our hybrid approach offers a thorough means to quantify and compare the morphologies of structurally diverse PA films,^{17,24,46,47} to eventually provide an insight on the relationship between the synthesis, morphology, and function of these filtration membranes, which has long awaited quantitative description. Such fundamental understanding could help unravel the mechanisms underlying nanoscale crumpling and manipulate it as nature does, in the brain, the gut, and lily leaves, to enhance performance.^{48–51} We also anticipate that the multitechnique approach we demonstrate is applicable to other nanostructured soft materials, such as polymer layers in photovoltaic and flow-cell devices,^{52–55} self-

assembled hierarchical membranes,^{3,56,57} or nanocomposites containing both hard (inorganic) and soft (organic/biological) components.^{58,59}

RESULTS AND DISCUSSION

A free-standing PA film was synthesized with modifications to a recent literature method¹⁷ (see the [Supporting Information](#) for details), via interfacial polymerization of trimesoyl chloride (TMC, 0.1 wt %) and *m*-phenylenediamine (MPD, 2 wt %) on a sacrificial layer of cadmium hydroxide nanostrands ([Figure 1a](#)). Gentle etching of the nanostrand layer leaves behind a free-floating PA film isolated from its polysulfone (PSf) support, and this film was gently scooped onto a TEM grid and then dried in air for imaging ([Figure 1b](#)). Low-dose ($7.4 \text{ e}^- \text{ \AA}^{-2} \text{ s}^{-1}$) electron tomography, where volumetric information is determined by collecting 2D projections from many different viewing angles,^{60,61} was used to reconstruct the crumpled morphology in 3D ([Figure 1c,d](#), see the [Supporting Information](#) for reconstruction details). As shown in [Figure 1e–g](#), a full 3D view of the crumpled film (crumple volumes in red) was reconstructed from 61 projections at varying tilt angles. In the reconstructed volume, the size of 1 voxel (i.e., one 3D pixel) is 6.8 Å. A typical cross-section of the raw reconstruction ([Figure 1e](#)), similar to those determined with microtomed samples in SEM or TEM^{25,29,36} shows that crumples extend outward from the flat part of the PA film. The crumples on the front side of the PA film are irregularly shaped and heterogeneous, leading to a root-mean-squared roughness of $18.0 \pm 0.4 \text{ nm}$ as measured by AFM ([Figures 1g and S1](#)). Unlike AFM or SEM, however, tomography reveals the full, 3D shape ([Figure 1f,h](#), and [Movie S1](#)). This raw reconstruction dataset, following additional image processing ([Figure S2](#), see details in the [Supporting Information](#)), was used for later analysis.

We first determined parameters directly related to film transport properties, such as the surface area and volume of crumples ([Figure 1h](#) in red), and the void space they enclose ([Figure 1h](#) in purple) to compare with bulk measurements performed routinely on PA films. From a tomographic dataset, these measurements can be performed essentially by counting the number of voxels and the number of exposed voxel faces, and the outer surface area to volume ratio describes how effectively crumples pack area into a given volume. Over 11 crumples, the area-to-volume ratio ranges from 0.09 to 0.18 nm^{-1} (see [Table S1](#) for complete results). Another parameter of note is how much crumpling actually enhances the amount of “functional” area relative to a flat film, particularly because a film’s permeance is proportional to its surface area.^{17,37,62} To evaluate this area enhancement, we compared the surface area of each crumple (A) with the area of its “footprint” (A_{fp} , i.e., the total area of the crumple’s base). For this film, the ratio between A and A_{fp} ranges between 3.5 and 15.7, suggesting that the permeance in crumpled regions of the film can be significantly enhanced. For example, taking recent results on the permeance of thin, flat films ($2.7 \text{ L m}^{-2} \text{ h}^{-1} \text{ bar}^{-1}$),⁶² crumpling on a scale similar to that observed here would lead to a permeance between 9.5 and 42.4 $\text{L m}^{-2} \text{ h}^{-1} \text{ bar}^{-1}$, assuming that film thickness and film cross-linking are unchanged. On the basis of the area-to-volume ratio and an estimate of the density of PA ($\sim 1.3 \text{ g cm}^{-3}$),³³ we also determined the average mass-per-area of crumples in the PA film ($1.1 \mu\text{g cm}^{-2}$, [Table S1](#)), which is otherwise measured using a quartz crystal microbalance or other bulk meth-

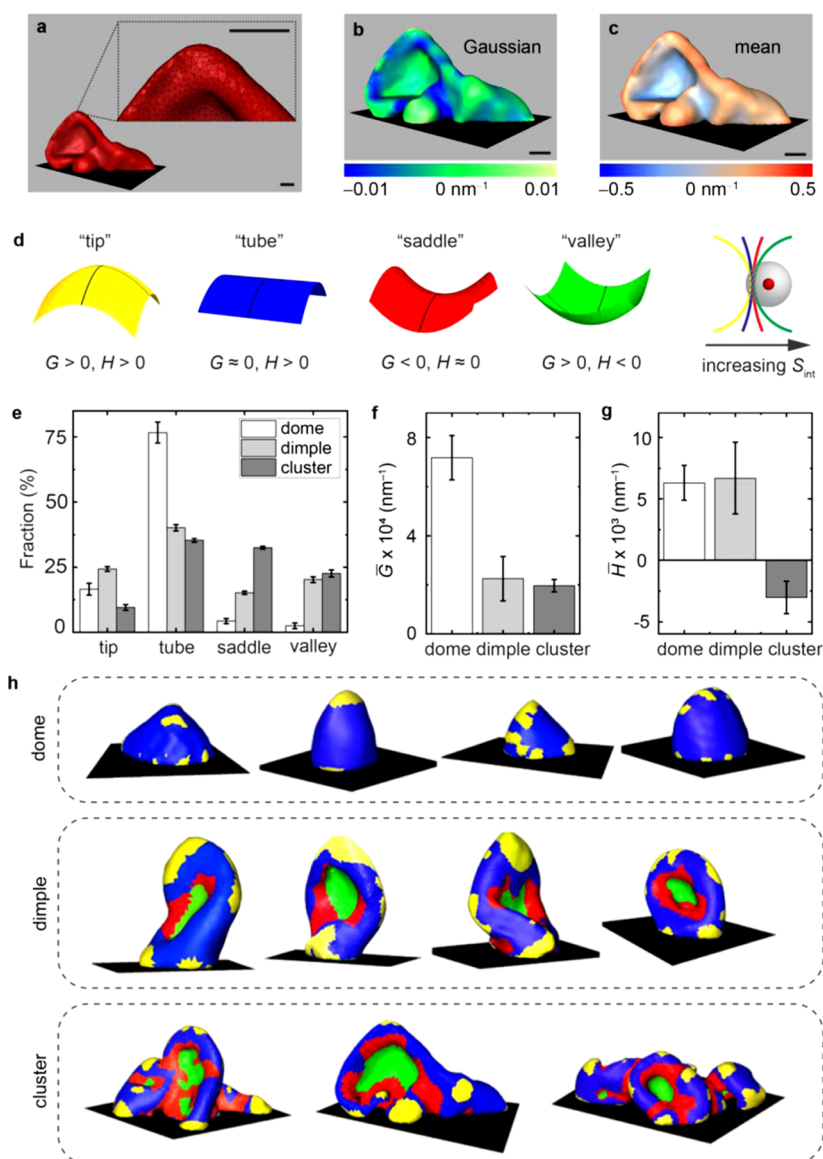


Figure 2. Local crumple curvature distribution divides the crumples into three groups. (a) Fully segmented crumples were converted into a triangulated surface mesh and color-coded according to local Gaussian curvature G (b) and mean curvature H (c) values at each mesh triangle. (d) G and H were used together to define four curvature elements. In the rightmost schematic, each of the four elements presents a different interaction area (denoted with the dotted portion of each curve) to an approaching solute (red dot) with a fixed interaction range (gray shadowed volume), with tips providing the least (yellow) and valley regions the most (green). (e) The relative abundance of different surface elements varies between crumple classes but is strongly consistent within a crumple class. Meanwhile, the average G (f) and H (g) can only distinguish one class from the two others. (h) Reconstructed volumes of dome, dimple, and cluster crumples as categorized based on (e), with surfaces colored according to the local curvature element (yellow: tip, blue: tube, red: saddle, green: valley). Scale bars: 50 nm.

ods.^{25,32,62} This value is comparable with recent bulk measurements ($2\text{--}4\ \mu\text{g cm}^{-2}$) for the same system.⁶² Geometric attributes of the voids enveloped by the PA crumple can also be measured directly from our reconstruction (Figures 1h and S3). Void space can be exposed to the back (water-facing) surface of the film (bottom void in Figure 1h, right) or be disconnected and fully enveloped by a film (top void in Figure 1h, right). We calculated that a single crumple can be between 4 and 30% void by volume (Figure S3 and Table S1), which is consistent with previous results^{19,25} and points to the importance of characterizing the substantial void space to understand the function of PA films.

Going beyond parameters that can be determined with macroscopic measurements, we next characterized the local

curvature of crumple surfaces. In the context of PA films, local nanoscale curvature serves as a quantitative description not only of the spatially varying morphology of crumples inaccessible to bulk measurements but also of the physicochemical interaction environments presented to solutes. For example, in a recent study it was found that by changing the local mean surface curvature from ~ 0.063 to $\sim 0.126\ \text{nm}^{-1}$, not only can the local charge density be increased by a factor of 2 but also the local pK_a of acidic ligands can decrease by $\sim 25\%$.⁶³ We analyzed local crumple curvatures by defining an arbitrary 3D shape, such as those adopted by the crumples, as a patchwork of four distinct curvature elements.³⁸ To do so, we first generated a triangulated mesh describing the outer surface of the reconstructed crumple (Figures 2a and S4) and then

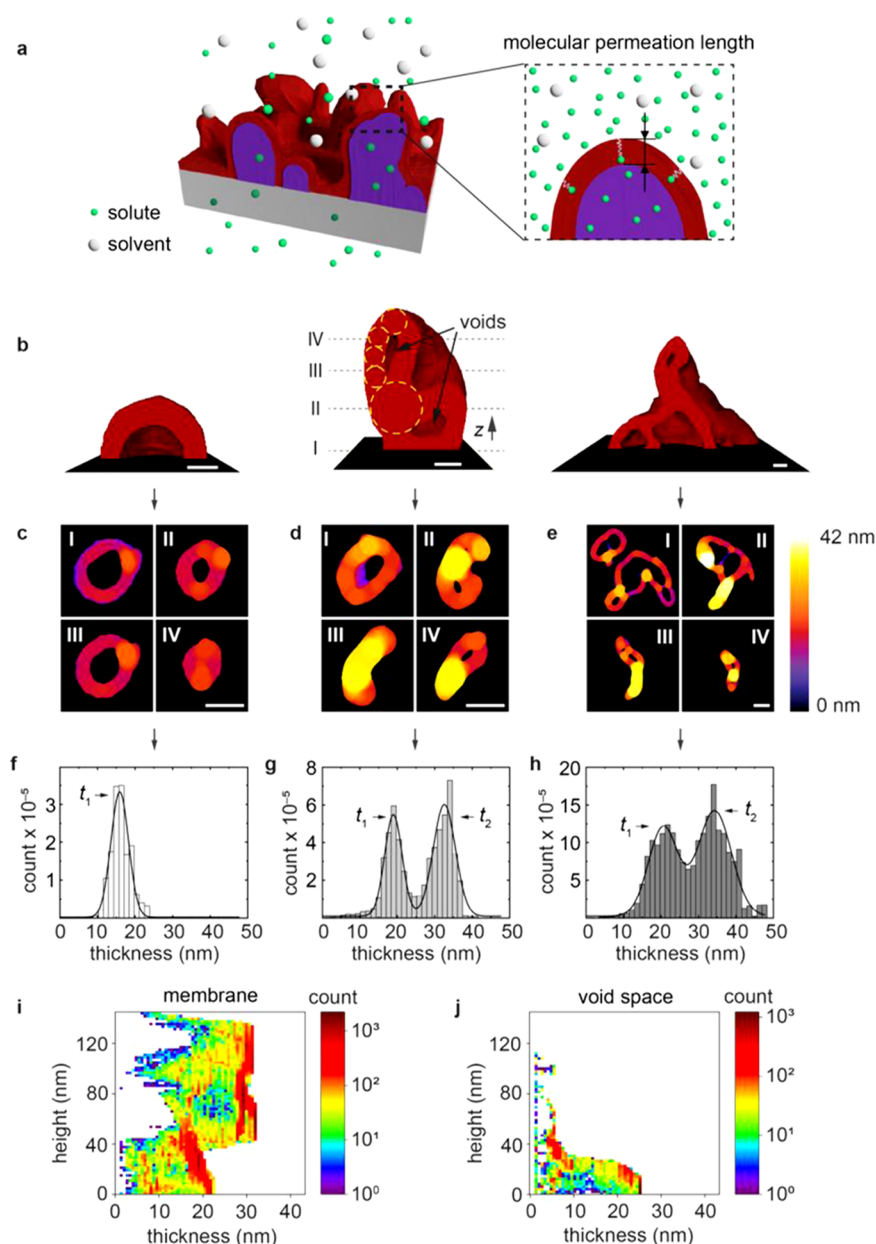


Figure 3. Local thickness of PA crumples. (a) Cartoon representation of solute and solvent filtration through a crumpled PA film, and a schematic depiction of the molecular permeation length across the membrane. (b) Representative cross-sections from each of the three crumple classes. Local thickness for each voxel point was defined as the size of the largest sphere that contains the point while remaining within the bounds of the crumple (see dotted yellow circles in the center). Note that the encompassing sphere need not be centered at a given point to describe the local thickness there. (c–e) xy slices through representative dome (c), dimpled (d), and cluster (e) crumples demonstrate that the local thickness varies considerably within the crumple, especially depending on whether the void is present at a given height. (f–h) Histograms of local thickness for each crumple type: domes (f), dimpled crumples (g), and clustered (h) crumples. (i, j) Distributions of local thickness of the membrane (i) and the void (j) volume in one dimpled crumple as a function of height reveal that the second peaks in the thickness distributions correspond to regions where the void has collapsed. Scale bars: 20 nm in (b), 50 nm in (c)–(e).

determined the two principal curvature values, κ_1 and κ_2 , at each surface triangle (the principal curvatures are defined as $1/R_1$ and $1/R_2$, where R_1 and R_2 are the radii of the smallest and largest spheres that can be fit to the surface at each point). Principal curvatures were then used to calculate the Gaussian curvature, G , the product of the two principal curvatures, and the mean curvature, H . The meshed crumple was rendered with each mesh triangle colored according to the local G (Figure 2b) and H (Figure 2c) values, which highlights the fluctuations in the local curvature across the crumple surface. The signs of G and H together define four different curvature

elements (Figure 2d): tip, tube, saddle, and valley regions.³⁸ In the context of filtration membranes, these surface elements present distinct interaction environments for a solute (represented schematically as a point-like red particle with a gray interaction range in Figure 2d, right) approaching the crumple surface; for a fixed interaction range, concave valleys provide the largest interaction area (S_{int}) and tips provide the smallest.

The relative abundance of the four curvature elements in each crumple, surprisingly, reveals that crumples fall quantitatively into three distinct classes (Figure 2e), despite

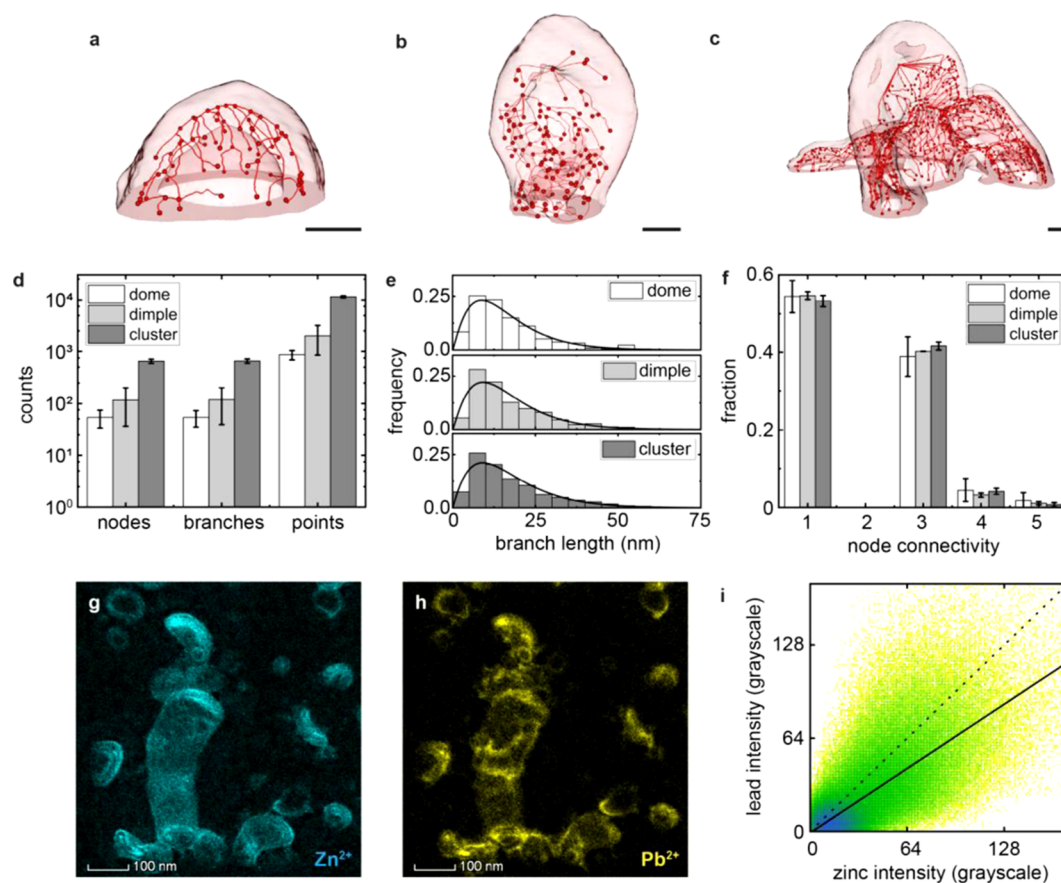


Figure 4. Skeletonization of crumples and elemental mapping of adsorbates on PA films. (a–c) Skeletonized versions of representative dome, dimpled, and cluster crumples, respectively, with nodes (red dots) connected by red branches. The complexity of the crumples, as described by the number of nodes, branches, and voxels in the skeleton, progressively increases, as shown in the semilog distribution plot (d). (e) The branch length distributions of the three crumple classes (top to bottom: domes, dimples, and clusters) are highly similar. The distributions of node connectivity (f) show the same consistency. (g, h) Elemental maps of Zn^{2+} (cyan) and Pb^{2+} (yellow) across a region of PA following ion adsorption. (i) Correlation of the intensities of zinc (g) and lead (h) maps. The dotted line is a hypothetical one describing perfect co-localization, whereas the black solid line was calculated from the experimental elemental maps and shows incomplete co-localization. Scale bars: 20 nm in (a)–(c), 100 nm in (g) and (h).

their apparent dissimilarities. Regarding morphology, these classes can be described qualitatively as hollow hemispherical domes, elongated dimples that collapse inward, and clusters that are more convoluted. Note that it is only when G and H are considered together that this distinction can be made (Figure 2e); the average Gaussian curvature, \bar{G} , of each crumple only distinguishes domes from dimples and clusters (Figure 2f), and the average mean curvature, \bar{H} , only distinguishes clusters from domes and dimples (Figure 2g). Shown in Figure 2h are renderings of the crumples sorted according to these classes, with surfaces color-coded according to the curvature element at each point on the triangular surface mesh. A number of details are worth noting. For example, compared to domes and dimples, clusters have a higher fraction of saddle elements ($\sim 32.3\%$) to connect their many convex tubes and concave valley domains (see Table S2 for complete data) and preserve the contiguity of the shape. Clusters also have the highest fraction of curvature element microenvironments favorable to solute adsorption: saddle and valley regions. Dimples, meanwhile, consist of predominantly tip and tube patches, and domes have mostly tube patches ($\sim 80\%$) with few saddle regions ($\sim 3.0\%$). This trend is preserved across the 11 crumples that we quantified, as indicated by the combined data (Figure 2e), which suggests

that there may be relatively few crumpling routes during PA film growth. Our quantification of crumple structures based on curvature elements also indicates a powerful tool to evaluate and compare PA films synthesized with diverse conditions,^{17,24,46,47} in terms of both their structure and the curvature environments they present during filtration processes.

Although the local curvature of the PA film influences the initial solute–crumple interactions during a filtration process, subsequent transmembrane diffusion (or rejection) is governed in part by the PA film thickness (Figure 3a).⁶⁴ We defined the local 3D thickness at each voxel in a crumple as the diameter of the largest sphere that can contain the voxel and remain within the bounds of the crumple (Figure 3b), which defines a transmembrane permeation path length not accessible by AFM measurements. Figure 3c–e shows xy cross-sections from crumples from each of the three classes, showing how the local thickness in 3D varies throughout a crumple (see also Movie S2). For example, the dome crumple has a fairly uniform local thickness from top to bottom, whereas dimples and clusters include one or more collapsed regions (e.g., Figure 3d,e, panels II–IV) thicker than void-containing regions, demonstrating the quantitative power of our measurements for a 3D film. We combined local thickness distributions according to the three

crumple classes we determined from curvature elements (Figures 3f–h and S5). Within each type, the local thickness distributions overlap reasonably well, validating the robustness of our crumple classification. Among the three classes, dome crumples have the smallest local thickness, suggesting a shorter permeation path for solvent molecules.

At the same time, the mapped local thicknesses exhibit a notable consistency. As shown in Figure 3f, dome crumples have a local thickness centered at 16 ± 5 nm, which is consistent with the thickness of the flat PA film regions measured by AFM (~ 16 nm, Figure S1). The more complex dimpled and cluster crumples have bimodal thickness distributions. The lower peak (t_1 in Figure 3g, 19 ± 5 nm) is comparable with the peak of domes, whereas the second peak is approximately twice t_1 ($t_2 = 33 \pm 6$ nm $\approx 2t_1$), indicating that the thicker regions correspond to those where two PA layers collapse inward. Indeed, using a dimpled crumple as an example, comparing the local thickness profile of the PA layer (Figure 3i) and void space (Figure 3j) inside the crumple as a function of z height reveals that void collapse (where the void thickness becomes zero) occurs where the approximately doubled thickness of the crumple appears (for additional examples, see Figure S6). Thus, a single PA layer thickness of approximately 15–20 nm explains all of the observed local thicknesses for the crumples. This observation is consistent with a crumpling mechanism where approximately uniform pieces of PA film are formed during the early stage of polymerization and local collapsing serves as the basis for the emergence of complicated 3D shapes observed here and in other PA films.²⁵ This crumpling mechanism has been hypothesized in previous work,^{19,23,24} and here we support it via quantitative morphology analysis.

In addition to the local morphology properties discussed above, we characterized single-crumple topological features, which quantify the overall shape complexity. Here, we used skeletonization,^{39,65} where a 3D crumple is iteratively thinned until only lines a single voxel thick remain while ensuring that no connectivity is lost. Figure 4a–c shows the skeletonization of representative dome, dimple, and cluster crumples, with nodes of the skeleton marked with dots, and lines between two adjacent nodes representing skeleton branches. As shown in Figure 4d, the crumple shape complexity increases from dome to dimple to cluster, as quantified by the number of nodes, branches, and points per skeleton, consistent with our characterizations above. Meanwhile, consistency also emerges. For example, skeleton branch lengths, regardless of crumple class, follow highly similar distributions (Figure 4e). In addition, the number of branches coming out of each node in the skeleton is distributed consistently for all crumples (Figure 4f), regardless of the crumple class. Namely, this consistency suggests a similar “density” of interconnectedness across all crumples. We speculate that the node connectivity is a parameter tunable by reaction parameters (reactant ratio, solvent, additives), and therefore another means of quantitatively comparing membranes prepared using different synthesis conditions.^{17,24,46,47}

Finally, as a demonstration of how nanoscopic crumpled structures in a PA film are coupled with solute adsorption, we used STEM-EDXS, an imaging technique which distinguishes elements by their characteristic X-ray emission spectra, to determine the spatial distributions of solutes after adsorption. Specifically, we chose Zn^{2+} and Pb^{2+} , which are metal ions left behind in the wastewater of many industrial processes.^{66,67}

They adsorb onto the PA film during incubation in an equimolar solution of $\text{Zn}(\text{NO}_3)_2$ and $\text{Pb}(\text{NO}_3)_2$. As shown in Figure 4g,h, the two ionic species have distinct local distributions; although zinc appears widely spread (Figure 4g), lead appears to exhibit site localization (Figure 4h). These differences in localization are also apparent from the imperfect correlation of zinc and lead across the entire image ($R \approx 0.77$, Figure 4i). We hypothesize that these differences in localization may be due to subtle hydration effects (e.g., differences in hydration energy, hydration radii, etc.) and may be related to the lower rejection of Pb^{2+} observed experimentally in bulk permeation tests with lead–zinc solutions.⁴⁵

CONCLUSIONS

In summary, using low-dose electron tomography and quantitative morphometry, we were able to map out functionally relevant, 3D features of PA crumples and the voids they enclose in a model separating layer system. In this example, our hybrid approach not only provides a means to extract a wide variety of transport-related properties from a single dataset; it also enables classification of a seemingly heterogeneous population of crumples into three types of microenvironments. This classification scheme suggests a quantitative way to distinguish diverse PA films^{17,24,46,47} and has implications for modeling membrane transport.²⁶ Meanwhile, features such as the local film thickness and node interconnectivity suggest common aspects of an underlying crumpling mechanism, and future quantitative morphometry studies on intermediate products may help unravel important details about how these structures actually develop during interfacial polymerization. Finally, elemental mapping of heavy metal adsorbates on the PA film demonstrates an interplay between nanoscale film structure, as quantified here, and film–solute interactions, which may serve as a connection between the physicochemical properties of solutes and their filtration behavior. More broadly, this combined imaging–analysis platform provides a powerful probe of soft material morphologies developed from molecular synthesis and a system to understand their complex nanoscale features in the context of function and performance.

METHODS AND EXPERIMENTAL DETAILS

Membrane Synthesis. A hydrated PSf substrate was fixed on a glass filter funnel. Methanol was filtered through the PSf, followed by nanopure water. Cadmium hydroxide nanowires were synthesized by sequential addition of aqueous solutions of $\text{CdCl}_2 \cdot \text{H}_2\text{O}$ (50 mL, 4 mM) and ethanolamine (50 mL, 2 mM) to a 250 mL Erlenmeyer flask stirring at 500 rpm at room temperature. The solution of cadmium hydroxide nanowires was filtered across the PSf substrate with a vacuum pump. Immediately after the nanowire solution was filtered across the PSf, an aqueous solution of MPD (25 mL, 2 wt %) was gently transferred onto the PSf substrate. TMC in hexanes (25 mL, 0.1 wt %) was added and was left on the PSf for 1 min. Then, the reaction was terminated by gently removing the TMC solution. Pure hexanes (10 mL) were added onto the PSf and removed immediately to rinse away any residual TMC. The PSf was rinsed with hexanes two more times. PSf with the polymerized PA film on top was placed in a Petri dish with water for one additional rinsing step and then transferred to another dish containing 10 mM hydrochloric acid. The PA film was released from the PSf after about 30 min due to the etching of the cadmium hydroxide nanowires by hydrochloric acid.

PA Film Characterization. A JEOL 2100 Cryo or JEOL 2010 LaB₆ TEM operating at 200 kV was used for imaging PA film morphology. The roughness of PA films was measured using tapping-mode atomic force microscopy (AFM, Asylum Research Cypher). A

series of tilt images of a PA film were acquired manually using a JEOL 2100 Cryo TEM. A low electron beam dose rate ($7.4 \text{ e}^- \text{ \AA}^{-2} \text{ s}^{-1}$) was applied using spot size 3. Each image was collected with a 3 s exposure time, resulting in a dose per image of $22.2 \text{ e}^- \text{ \AA}^{-2}$. The tilt angle ranged from -60 to 60° in 2° increments. IMOD 4.9.3 (University of Colorado, <http://bio3d.colorado.edu/>) was used to align and assemble TEM images.⁶⁸ Since no fiducial markers were used, a patch tracking mode was applied, and the tomogram was generated using the standard weighted back-projection algorithm available in IMOD. Segmentation and 3D morphology analyses were performed in ImageJ/FIJI⁶⁹ and Amira 6.4⁷⁰ (FEI).

Ion Adsorption and STEM-EDXS. A small piece of PA film was transferred to a Petri dish containing 5 mL water to draw off residual hydrochloric acid and any other chemicals from the synthesis. Then, the water was removed using a micropipette, and an aqueous solution of metal salts (5 mL of 540 mM $\text{Pb}(\text{NO}_3)_2$ and 5 mL of 540 mM $\text{Zn}(\text{NO}_3)_2$) was added to the Petri dish. The PA film was incubated in salt solution for 24 h. Then, the metal solution was removed, and 5 mL of fresh water was added to the Petri dish to rinse off excess salt. The film was quickly scooped onto a TEM grid (Quantifoil R 1/4 Holey Carbon, 300 Mesh, Gold, Electron Microscopy Sciences). The grid was dried at room temperature before imaging. EDXS was performed on an FEI Talos F200X TEM/STEM with a field emission gun and a SuperX energy-dispersive spectrometer and an FEI Tecnai F20ST TEM/STEM at an accelerating voltage of 200 kV.

■ ASSOCIATED CONTENT

Supporting Information

The Supporting Information is available free of charge on the ACS Publications website at DOI: 10.1021/acsami.8b20826.

Chemicals; Synthesis and characterization of PA films with AFM, TEM, and STEM-EDXS; Image processing and 3D morphometry methods (PDF)

Movie S1, animated 3D rendering and slices through the reconstructed membrane (AVI)

Movie S2, slices and distributions showing the variation of local thickness throughout representative dome, dimple, and cluster crumples (AVI)

■ AUTHOR INFORMATION

Corresponding Author

*E-mail: qchen20@illinois.edu.

ORCID

Hyosung An: 0000-0001-8710-1012

Jordan M. Dennison: 0000-0001-9766-1048

Qian Chen: 0000-0002-1968-441X

Present Address

[†]Department of Chemistry and Research Institute of Natural Sciences, Gyeongsang National University, Jinju 52828, Republic of Korea (J.K.).

Author Contributions

[†]X.S. and J.W.S. contributed equally to this work.

Notes

The authors declare no competing financial interest.

■ ACKNOWLEDGMENTS

The authors would like to acknowledge funding and technical support from BP through the BP International Centre for Advanced Materials (BP-ICAM) which made the membrane synthesis, electron tomography, and element mapping experiments possible. Image analysis and morphometry components of this work were funded under the Air Force Office of Scientific Research Young Investigator Program (AFOSR-YIP)

project FA9550-17-1-0296. This research also used resources at the Center for Nanoscale Materials, an Office of Science user facility, supported in part by Laboratory Directed Research Development (LDRD) funding at Argonne National Laboratory, provided by the Director, Office of Science, of the U.S. Department of Energy under Contract No. DE-AC02-06CH11357. The authors also thank Dr. Lin Ming at the Institute of Materials Research and Engineering (IMRE), Singapore, and Janet Sinn-Hanlon at the College of Veterinary Medicine, University of Illinois Urbana-Champaign, for their help with tomography 3D reconstruction.

■ REFERENCES

- (1) Nunes, S. P.; Behzad, A. R.; Hooghan, B.; Sougrat, R.; Karunakaran, M.; Pradeep, N.; Vainio, U.; Peinemann, K.-V. Switchable pH-Responsive Polymeric Membranes Prepared via Block Copolymer Micelle Assembly. *ACS Nano* **2011**, *5*, 3516–3522.
- (2) O'Reilly, R. K.; Hawker, C. J.; Wooley, K. L. Cross-Linked Block Copolymer Micelles: Functional Nanostructures of Great Potential and Versatility. *Chem. Soc. Rev.* **2006**, *35*, 1068–1083.
- (3) Xu, T.; Zhao, N.; Ren, F.; Hourani, R.; Lee, M. T.; Shu, J. Y.; Mao, S.; Helms, B. A. Subnanometer Porous Thin Films by the Co-Assembly of Nanotube Subunits and Block Copolymers. *ACS Nano* **2011**, *5*, 1376–1384.
- (4) Shin, D. O.; Mun, J. H.; Hwang, G.-T.; Yoon, J. M.; Kim, J. Y.; Yun, J. M.; Yang, Y.-B.; Oh, Y.; Lee, J. Y.; Shin, J.; Lee, K. J.; Park, S.; Kim, J. U.; Kim, S. O. Multicomponent Nanopatterns by Directed Block Copolymer Self-Assembly. *ACS Nano* **2013**, *7*, 8899–8907.
- (5) Gotrik, K. W.; Hannon, A. F.; Son, J. G.; Keller, B.; Alexander-Katz, A.; Ross, C. A. Morphology Control in Block Copolymer Films Using Mixed Solvent Vapors. *ACS Nano* **2012**, *6*, 8052–8059.
- (6) Feng, H.; Lu, X.; Wang, W.; Kang, N.-G.; Mays, J. Block Copolymers: Synthesis, Self-Assembly, and Applications. *Polymers* **2017**, *9*, No. 494.
- (7) Kondo, S.; Miura, T. Reaction–Diffusion Model as a Framework for Understanding Biological Pattern Formation. *Science* **2010**, *329*, 1616–1620.
- (8) Cera, L.; Schalley, C. A. Under Diffusion Control: From Structuring Matter to Directional Motion. *Adv. Mater.* **2018**, *30*, No. 1707029.
- (9) Gordon, R.; Losic, D.; Tiffany, M. A.; Nagy, S. S.; Sterrenburg, F. A. S. The Glass Menagerie: Diatoms for Novel Applications in Nanotechnology. *Trends Biotechnol.* **2009**, *27*, 116–127.
- (10) Liu, B.; Zeng, H. C. Symmetric and Asymmetric Ostwald Ripening in the Fabrication of Homogeneous Core–Shell Semiconductors. *Small* **2005**, *1*, 566–571.
- (11) Teo, J. J.; Chang, Y.; Zeng, H. C. Fabrications of Hollow Nanocubes of Cu_2O and Cu via Reductive Self-Assembly of CuO Nanocrystals. *Langmuir* **2006**, *22*, 7369–7377.
- (12) Kaplan, C. N.; Noorduyn, W. L.; Li, L.; Sadza, R.; Folkertsma, L.; Aizenberg, J.; Mahadevan, L. Controlled Growth and Form of Precipitating Microsculptures. *Science* **2017**, *355*, 1395–1399.
- (13) Marchetti, P.; Peeva, L.; Livingston, A. The Selectivity Challenge in Organic Solvent Nanofiltration: Membrane and Process Solutions. *Annu. Rev. Chem. Biomol. Eng.* **2017**, *8*, 473–497.
- (14) Marchetti, P.; Jimenez Solomon, M. F.; Szekeley, G.; Livingston, A. G. Molecular Separation with Organic Solvent Nanofiltration: A Critical Review. *Chem. Rev.* **2014**, *114*, 10735–10806.
- (15) Vandezande, P.; Gevers, L. E. M.; Vankelecom, I. F. J. Solvent Resistant Nanofiltration: Separating on a Molecular Level. *Chem. Soc. Rev.* **2008**, *37*, 365–405.
- (16) Chan, W.-F.; Chen, H.; Surapathi, A.; Taylor, M. G.; Shao, X.; Marand, E.; Johnson, J. K. Zwitterion Functionalized Carbon Nanotube/Polyamide Nanocomposite Membranes for Water Desalination. *ACS Nano* **2013**, *7*, 5308–5319.
- (17) Karan, S.; Jiang, Z.; Livingston, A. G. Sub–10 nm Polyamide Nanofilms with Ultrafast Solvent Transport for Molecular Separation. *Science* **2015**, *348*, 1347–1351.

- (18) Cahill, D. G.; Freger, V.; Kwak, S.-Y. Microscopy and Microanalysis of Reverse-Osmosis and Nanofiltration Membranes. *MRS Bull.* **2008**, *33*, 27–32.
- (19) Yan, H.; Miao, X.; Xu, J.; Pan, G.; Zhang, Y.; Shi, Y.; Guo, M.; Liu, Y. The Porous Structure of the Fully-Aromatic Polyamide Film in Reverse Osmosis Membranes. *J. Membr. Sci.* **2015**, *475*, 504–510.
- (20) Tsuru, T.; Sasaki, S.; Kamada, T.; Shintani, T.; Ohara, T.; Nagasawa, H.; Nishida, K.; Kanezashi, M.; Yoshioka, T. Multilayered Polyamide Membranes by Spray-Assisted 2-Step Interfacial Polymerization for Increased Performance of Trimesoyl Chloride (TMC)/m-Phenylenediamine (MPD)-Derived Polyamide Membranes. *J. Membr. Sci.* **2013**, *446*, 504–512.
- (21) Wijmans, J. G.; Baker, R. W. The Solution-Diffusion Model: A Review. *J. Membr. Sci.* **1995**, *107*, 1–21.
- (22) Geise, G. M.; Park, H. B.; Sagle, A. C.; Freeman, B. D.; McGrath, J. E. Water Permeability and Water/Salt Selectivity Tradeoff in Polymers for Desalination. *J. Membr. Sci.* **2011**, *369*, 130–138.
- (23) Xu, J.; Yan, H.; Zhang, Y.; Pan, G.; Liu, Y. The Morphology of Fully-Aromatic Polyamide Separation Layer and Its Relationship with Separation Performance of TFC Membranes. *J. Membr. Sci.* **2017**, *541*, 174–188.
- (24) Hirose, M.; Ito, H.; Kamiyama, Y. Effect of Skin Layer Surface Structures on the Flux Behaviour of RO Membranes. *J. Membr. Sci.* **1996**, *121*, 209–215.
- (25) Lin, L.; Lopez, R.; Ramon, G. Z.; Coronell, O. Investigating the Void Structure of the Polyamide Active Layers of Thin-Film Composite Membranes. *J. Membr. Sci.* **2016**, *497*, 365–376.
- (26) Wong, M. C. Y.; Lin, L.; Coronell, O.; Hoek, E. M. V.; Ramon, G. Z. Impact of Liquid-Filled Voids within the Active Layer on Transport through Thin-Film Composite Membranes. *J. Membr. Sci.* **2016**, *500*, 124–135.
- (27) Petersen, R. J. Composite Reverse Osmosis and Nanofiltration Membranes. *J. Membr. Sci.* **1993**, *83*, 81–150.
- (28) Kwak, S.-Y.; Jung, S. G.; Yoon, Y. S.; Ihm, D. W. Details of Surface Features in Aromatic Polyamide Reverse Osmosis Membranes Characterized by Scanning Electron and Atomic Force Microscopy. *J. Polym. Sci., Part B: Polym. Phys.* **1999**, *37*, 1429–1440.
- (29) Pacheco, F.; Sougrat, R.; Reinhard, M.; Leckie, J. O.; Pinnau, I. 3D Visualization of the Internal Nanostructure of Polyamide Thin Films in RO Membranes. *J. Membr. Sci.* **2016**, *501*, 33–44.
- (30) Sun, C.; Xie, L.; Li, X.; Sun, L.; Dai, H. Study on Different Ultrafiltration-Based Hybrid Pretreatment Systems for Reverse Osmosis Desalination. *Desalination* **2015**, *371*, 18–25.
- (31) Freger, V.; Bottino, A.; Capannelli, G.; Perry, M.; Gitis, V.; Belfer, S. Characterization of Novel Acid-Stable NF Membranes before and after Exposure to Acid Using ATR-FTIR, TEM and AFM. *J. Membr. Sci.* **2005**, *256*, 134–142.
- (32) Foglia, F.; Karan, S.; Nania, M.; Jiang, Z.; Porter, A. E.; Barker, R.; Livingston, A. G.; Cabral, J. T. Neutron Reflectivity and Performance of Polyamide Nanofilms for Water Desalination. *Adv. Funct. Mater.* **2017**, *27*, No. 1701738.
- (33) Lin, L.; Feng, C.; Lopez, R.; Coronell, O. Identifying Facile and Accurate Methods to Measure the Thickness of the Active Layers of Thin-Film Composite Membranes – A Comparison of Seven Characterization Techniques. *J. Membr. Sci.* **2016**, *498*, 167–179.
- (34) Zhang, X.; Settembre, E.; Xu, C.; Dormitzer, P. R.; Bellamy, R.; Harrison, S. C.; Grigorieff, N. Near-Atomic Resolution Using Electron Cryomicroscopy and Single-Particle Reconstruction. *Proc. Natl. Acad. Sci. U.S.A.* **2008**, *105*, 1867–1872.
- (35) Wan, W.; Briggs, J. A. G. Cryo-Electron Tomography and Subtomogram Averaging. In *Methods in Enzymology*. In *The Resolution Revolution: Recent Advances in cryoEM*; Crowther, R. A., Ed.; Academic Press, 2016; Chapter 13, Vol. 579, pp 329–367.
- (36) Klosowski, M. M.; McGilvery, C. M.; Li, Y.; Abellan, P.; Ramasse, Q.; Cabral, J. T.; Livingston, A. G.; Porter, A. E. Micro-to Nano-Scale Characterisation of Polyamide Structures of the SW30HR RO Membrane Using Advanced Electron Microscopy and Stain Tracers. *J. Membr. Sci.* **2016**, *520*, 465–476.
- (37) Culp, T. E.; Shen, Y.; Geitner, M.; Paul, M.; Roy, A.; Behr, M. J.; Rosenberg, S.; Gu, J.; Kumar, M.; Gomez, E. D. Electron Tomography Reveals Details of the Internal Microstructure of Desalination Membranes. *Proc. Natl. Acad. Sci. U.S.A.* **2018**, 8694–8699.
- (38) Elliott, H.; Fischer, R. S.; Myers, K. A.; Desai, R. A.; Gao, L.; Chen, C. S.; Adelstein, R. S.; Waterman, C. M.; Danuser, G. Myosin II Controls Cellular Branching Morphogenesis and Migration in Three Dimensions by Minimizing Cell-Surface Curvature. *Nat. Cell Biol.* **2015**, *17*, 137–147.
- (39) Fouard, C.; Malandain, G.; Prohaska, S.; Westerhoff, M. Blockwise Processing Applied to Brain Microvascular Network Study. *IEEE Trans. Med. Imaging* **2006**, *25*, 1319–1328.
- (40) Dougherty, R.; Kunzelmann, K.-H. Computing Local Thickness of 3D Structures with ImageJ. *Microsc. Microanal.* **2007**, *13*, 1678–1679.
- (41) Zaluzec, N. J. Processing and Quantification of X-Ray Energy-Dispersive Spectra in the Analytical Electron Microscope. *Ultra-microscopy* **1989**, *28*, 226–235.
- (42) Lewis, E. A.; Haigh, S. J.; Slater, T. J. A.; He, Z.; Kulzick, M. A.; Burke, M. G.; Zaluzec, N. J. Real-Time Imaging and Local Elemental Analysis of Nanostructures in Liquids. *Chem. Commun.* **2014**, *50*, 10019–10022.
- (43) Zaluzec, N. J.; Burke, M. G.; Haigh, S. J.; Kulzick, M. A. X-Ray Energy-Dispersive Spectrometry during in Situ Liquid Cell Studies Using an Analytical Electron Microscope. *Microsc. Microanal.* **2014**, *20*, 323–329.
- (44) Strathmann, H. Membrane Separation Processes. *J. Membr. Sci.* **1981**, *9*, 121–189.
- (45) Mehdipour, S.; Vatanpour, V.; Kariminia, H.-R. Influence of Ion Interaction on Lead Removal by a Polyamide Nanofiltration Membrane. *Desalination* **2015**, *362*, 84–92.
- (46) Duan, M.; Wang, Z.; Xu, J.; Wang, J.; Wang, S. Influence of Hexamethyl Phosphoramide on Polyamide Composite Reverse Osmosis Membrane Performance. *Sep. Purif. Technol.* **2010**, *75*, 145–155.
- (47) Kwak, S.-Y.; Woo Ihm, D. Use of Atomic Force Microscopy and Solid-State NMR Spectroscopy to Characterize Structure–Property–Performance Correlation in High-Flux Reverse Osmosis (RO) Membranes. *J. Membr. Sci.* **1999**, *158*, 143–153.
- (48) Savin, T.; Kurpios, N. A.; Shyer, A. E.; Florescu, P.; Liang, H.; Mahadevan, L.; Tabin, C. J. On the Growth and Form of the Gut. *Nature* **2011**, *476*, 57–62.
- (49) Tallinen, T.; Chung, J. Y.; Rousseau, F.; Girard, N.; Lefevre, J.; Mahadevan, L. On the Growth and Form of Cortical Convulsions. *Nat. Phys.* **2016**, *12*, 588–593.
- (50) Tsukaya, H. Mechanism of Leaf-Shape Determination. *Annu. Rev. Plant Biol.* **2006**, *57*, 477–496.
- (51) LoPresti, C.; Massignani, M.; Ferynhough, C.; Blanazs, A.; Ryan, A. J.; Madsen, J.; Warren, N. J.; Armes, S. P.; Lewis, A. L.; Chirasatitsin, S.; Engler, A. J.; Battaglia, G. Controlling Polymersome Surface Topology at the Nanoscale by Membrane Confined Polymer/Polymer Phase Separation. *ACS Nano* **2011**, *5*, 1775–1784.
- (52) Nasti, G.; Sanchez, S.; Gunkel, I.; Balog, S.; Roose, B.; Wilts, B. D.; Teuscher, J.; Gentile, G.; Cerruti, P.; Ambrogio, V.; Carfagna, C.; Steiner, U.; Abate, A. Patterning of Perovskite–Polymer Films by Wrinkling Instabilities. *Soft Matter* **2017**, *13*, 1654–1659.
- (53) Kim, J. B.; Kim, P.; Pégard, N. C.; Oh, S. J.; Kagan, C. R.; Fleischer, J. W.; Stone, H. A.; Loo, Y.-L. Wrinkles and Deep Folds as Photonic Structures in Photovoltaics. *Nat. Photonics* **2012**, *6*, 327–332.
- (54) He, M.; Wang, M.; Lin, C.; Lin, Z. Optimization of Molecular Organization and Nanoscale Morphology for High Performance Low Bandgap Polymer Solar Cells. *Nanoscale* **2014**, *6*, 3984–3994.
- (55) Haldrup, S.; Catalano, J.; Hinge, M.; Jensen, G. V.; Pedersen, J. S.; Bienten, A. Tailoring Membrane Nanostructure and Charge Density for High Electrokinetic Energy Conversion Efficiency. *ACS Nano* **2016**, *10*, 2415–2423.

(56) Zha, R. H.; Velichko, Y. S.; Bitton, R.; Stupp, S. I. Molecular Design for Growth of Supramolecular Membranes with Hierarchical Structure. *Soft Matter* **2016**, *12*, 1401–1410.

(57) Rancatore, B. J.; Mauldin, C. E.; Tung, S.-H.; Wang, C.; Hexemer, A.; Strzalka, J.; Fréchet, J. M. J.; Xu, T. Nanostructured Organic Semiconductors via Directed Supramolecular Assembly. *ACS Nano* **2010**, *4*, 2721–2729.

(58) Zhang, J.; Santos, P. J.; Gabrys, P. A.; Lee, S.; Liu, C.; Macfarlane, R. J. Self-Assembling Nanocomposite Tectons. *J. Am. Chem. Soc.* **2016**, *138*, 16228–16231.

(59) Bai, P.; Yang, S.; Bao, W.; Kao, J.; Thorkelsson, K.; Salmeron, M.; Zhang, X.; Xu, T. Diversifying Nanoparticle Assemblies in Supramolecule Nanocomposites via Cylindrical Confinement. *Nano Lett.* **2017**, *17*, 6847–6854.

(60) Ercius, P.; Weyland, M.; Muller, D. A.; Gignac, L. M. Three-Dimensional Imaging of Nanovoids in Copper Interconnects Using Incoherent Bright Field Tomography. *Appl. Phys. Lett.* **2006**, *88*, No. 243116.

(61) Scott, M. C.; Chen, C.-C.; Mecklenburg, M.; Zhu, C.; Xu, R.; Ercius, P.; Dahmen, U.; Regan, B. C.; Miao, J. Electron Tomography at 2.4-Ångström Resolution. *Nature* **2012**, *483*, 444–447.

(62) Jiang, Z.; Karan, S.; Livingston, A. G. Water Transport through Ultrathin Polyamide Nanofilms Used for Reverse Osmosis. *Adv. Mater.* **2018**, *30*, No. 1705973.

(63) Walker, D. A.; Leitsch, E. K.; Nap, R. J.; Szleifer, I.; Grzybowski, B. A. Geometric Curvature Controls the Chemical Patchiness and Self-Assembly of Nanoparticles. *Nat. Nanotechnol.* **2013**, *8*, 676–681.

(64) Gorgojo, P.; Karan, S.; Wong, H. C.; Jimenez-Solomon, M. F.; Cabral, J. T.; Livingston, A. G. Ultrathin Polymer Films with Intrinsic Microporosity: Anomalous Solvent Permeation and High Flux Membranes. *Adv. Funct. Mater.* **2014**, *24*, 4729–4737.

(65) Pudney, C. Distance-Ordered Homotopic Thinning: A Skeletonization Algorithm for 3D Digital Images. *Comput. Vis. Image Understanding* **1998**, *72*, 404–413.

(66) Babel, S.; Kurniawan, T. A. Cr(VI) Removal from Synthetic Wastewater Using Coconut Shell Charcoal and Commercial Activated Carbon Modified with Oxidizing Agents and/or Chitosan. *Chemosphere* **2004**, *54*, 951–967.

(67) Prakash, S.; Kumar, M.; Tripathi, B. P.; Shahi, V. K. Sol–Gel Derived Poly(Vinyl Alcohol)-3-(2-Aminoethylamino) Propyl Trimethoxysilane: Cross-Linked Organic–Inorganic Hybrid Beads for the Removal of Pb(II) from Aqueous Solution. *Chem. Eng. J.* **2010**, *162*, 28–36.

(68) Kremer, J. R.; Mastrorarde, D. N.; McIntosh, J. R. Computer Visualization of Three-Dimensional Image Data Using IMOD. *J. Struct. Biol.* **1996**, *116*, 71–76.

(69) Schindelin, J.; Arganda-Carreras, I.; Frise, E.; Kaynig, V.; Longair, M.; Pietzsch, T.; Preibisch, S.; Rueden, C.; Saalfeld, S.; Schmid, B.; Tinevez, J. Y.; White, D. J.; Hartenstein, V.; Eliceiri, K.; Tomancak, P.; Cardona, A. Fiji: An Open-Source Platform for Biological-Image Analysis. *Nat. Methods* **2012**, *9*, 676–682.

(70) Stalling, D.; Westerhoff, M.; Hege, H.-C. *Amira: A Highly Interactive System for Visual Data Analysis*; Elsevier, 2005; pp 749–769.